LARGE-EDDY SIMULATION OF SCALAR MIXING IN THE TURBULENT WAKE OF A SQUARE CYLINDER

Guido Lodato
Department of Energy and Propulsion
INSA de Rouen – UMR 6614 CORIA, France
guido.lodato@insa-rouen.fr

Riccardo Rossi
Dipartimento di Ingegneria Industriale
Università di Bologna
Viale Risorgimento 2, 40136 Bologna, Italy
riccardo.rossi12@unibo.it

ABSTRACT

Numerical experiments by Large-Eddy Simulation (LES) are performed on the turbulent flow and mixing of a passive scalar past a square cylinder. A Reynolds number of 21 400 is selected, matching available flow measurements from laser-doppler velocimetry (LDV), and the scalar released from a point source downstream of the cylinder. A comparative study of numerical results against LDV data is presented in order to validate the present LES methodology, where subgrid turbulent stresses are estimated via the WALE similarity mixed model coupled with newly developed constrained filtering operators of arbitrary order and scalar fluxes approximated via the Reynolds analogy. Time-averaged and phase-averaged statistics for the scalar field, including scalar variance and scalar flux components, are computed to examine further the role of coherent fluctuations associated with large-scale structures on the mixing process and to establish a database for turbulence models development and validation.

INTRODUCTION

The numerical simulation of mixing downstream of bluff bodies displaying an unsteady turbulent wake is particularly challenging because of the need for representing not only the turbulent transport associated with random or irregular fluctuations, for which most of turbulence models are designed for, but also the effect of large-scale coherent structures on the mixing process.

For example, laboratory experiments performed with thermal wakes developing from heated cylinders in cross flow (Matsumura & Antonia, 1993; Yiu *et al.*, 2004) addressed the impact of vortex-shedding in the transport of heat and clarified the role of periodic and random fluctuations, where coherent structures were found acting to entrain the cold fluid from the free stream into the wake developing region, whereas the transport of heat out of the vortices was dominated by turbulent fluctuations. In the case of scalar dispersion from localized sources located near bluff bodies, it is also well established that the decay rate of scalar concentration and the plume spread are considerably affected by the onset of plume meandering (Brown, 1987; Tsunoda *et al.*, 1993).

From the modeling perspective of the RANS equations, most of the effort has been dedicated to the prediction of the flow field and to the modeling of the Reynolds stress tensor (Bosch & Rodi, 1998; Lakehal & Thiele, 2000; Ramesh *et al.*, 2006). Nonetheless, numerical experiments based on Direct Numerical Simulations (DNS) show some differences between the dynamics of the velocity and scalar fields when coherent large-scale structures develop downstream of a bluff body (Djenidi & Antonia, 2009), suggesting the need for extending the analysis to the modeling of the scalar field.

A first attempt in RANS modeling of turbulent mixing in an unsteady wake was presented in Rossi & Iaccarino (2013), where steady and unsteady RANS simulations based on the standard gradient-diffusion hypothesis (SGDH) for the scalar fluxes have been validated against DNS statistics for the case of dispersion from a point source located on top of a wall mounted cube. The unsteady RANS model (URANS), by resolving explicitly the dominant frequency of the vortex shedding and plume meandering downstream of the cube, was found able to give a representation of turbulent transport consistent with DNS data, resulting in better prediction of the plume spread and decay rate of scalar concentration. However, the comparative study was limited by the onset of a low-frequency modulation in the unsteady wake as well as by the computational cost required by computing long term statistics from DNS.

In this contribution, Large-Eddy Simulations (LES) are performed for the mixing of a passive scalar downstream of a square cylinder. This particular setup is chosen to establish flow conditions where periodic oscillations in the wake of the bluff body display a dominant frequency, thereby allowing for a better evaluation of modeling strategies for the scalar field. Furthermore, using LES the computational effort required to compute long term statistics will be eased, making possible to obtain phase-averaged statistics which are particularly useful in determining the relative contribution of coherent and random fluctuations on turbulent transport and its implications for the scalar flux modeling.

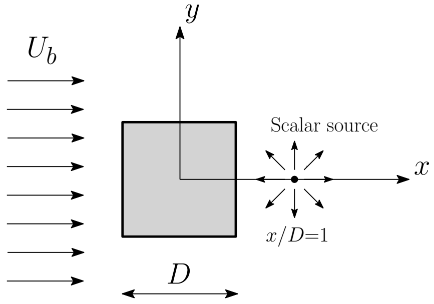

Figure 1. Sketch of flow setup.

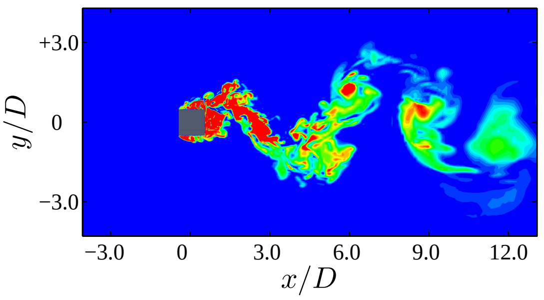

Figure 2. Snapshot of normalized scalar concentration $c/C_{\max}$ downstream of the cylinder, contour range $0 \div 1 \times 10^{-1}$.

FLOW SETUP AND CONDITIONS

A sketch of the present flow setup is shown in Fig. 1. The square cylinder is placed in a uniform stream and the scalar released from a point source located on the symmetry plane at $x/D = 1$, where D is the size of the cylinder. A Reynolds number of 22 400, based on the free-stream velocity U_b and the size of the cylinder, is selected for the analysis in order to match the conditions in the experiment by Lyn & Rodi (1994) and Lyn *et al.* (1995), from which Laser Doppler Velocimetry (LDV) measurements are available. The Schimdt number of the scalar, which is passively transported by the flow, is set to 0.72 in the computations.

Fig. 2 presents a snapshot of the instantanous scalar field downstream of the cylinder. The scalar released by the point source, located within the mean separated region of the flow, is first alternatively convected upstream during the shedding cycle towards the windward side of the cylinder, marking the roll up of the shear layer developing from the leading edges of the bluff body. The scalar is then entrained in the vortex-street, also marked by the scalar field, where regions of high scalar concentration are found within the vortical structures in the wake of the cylinder up to x/D=9 in the picture.

NUMERICAL TECHNIQUE AND LES MODEL

The computations are performed using a high-order spectral difference scheme for unstructured meshes (Huynh, 2007; Sun *et al.*, 2007; Liang *et al.*, 2009; Vincent *et al.*, 2010) coupled with an explicit Runge-Kutta time integration scheme. This numerical platform is used to solve the filtered compressible Navier-Stokes equations. After introducing the fluid density ρ, the velocity u_i, the total energy e (internal + kinetic) and a transported scalar c, these are written as

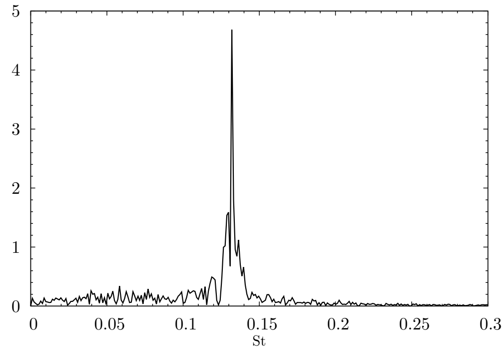

Figure 3. Discrete Fourier transform of the time history of the lift coefficient.

$$\partial_t \overline{\rho} + \partial_{x_j}(\overline{\rho u_j}) = 0 \quad (1)$$

$$\partial_t(\overline{\rho u_i}) + \partial_{x_j}(\overline{\rho}\widetilde{u}_i\widetilde{u}_j) + \partial_{x_i}\overline{\varpi} = \partial_{x_j}(2\overline{\mu}\widetilde{A}_{ij} + \tau^{\mathrm{d}}_{ij}) \quad (2)$$

$$\partial_t(\overline{\rho e}) + \partial_{x_j}[(\overline{\rho e} + \overline{\varpi})\widetilde{u}_j] = \partial_{x_j}(\overline{\Phi}_j + \overline{\lambda}\partial_{x_j}\widetilde{\vartheta} + q_j) \quad (3)$$

$$\partial_t(\overline{\rho c}) + \partial_{x_j}(\overline{\rho c}\widetilde{u}_j) = \partial_{x_j}(\overline{\rho}\overline{D}\partial_{x_j}\widetilde{c} + q^c_j) \quad (4)$$

where the *bar* filter operator and the Favre filter operator *tilde* have been used, μ is the dynamic viscosity, A_{ij} is the deviator of the deformation tensor and $\overline{\Phi}_j = 2\overline{\mu}\widetilde{u}_k\widetilde{A}_{jk}$. The thermal conductivity and the diffusion coefficient are computed from the Prandtl and Schmidt numbers as $\overline{\lambda} = \overline{\mu}c_p/Pr$ and $\overline{D} = \overline{\mu}/(\overline{\rho}Sc)$, with $Pr = Sc = 0.72$. The macro-pressure $\overline{\varpi}$ and macro-temperature $\widetilde{\vartheta}$ are related by the usual equation of state, $\overline{\varpi} = \overline{\rho}R\widetilde{\vartheta}$, where R represents the gas constant. The unclosed SGS terms τ_{ij} and q_j ('d' refers to the deviatoric part of the relevant tensor) are modeled according to the WALE Similarity Mixed (WSM) model (Lodato *et al.*, 2009),

$$\tau^{\mathrm{d}}_{ij} = 2\overline{\rho}\nu_{\mathrm{sgs}}\widetilde{A}_{ij} - \overline{\rho}\left(\widehat{\widetilde{u}_i\widetilde{u}_j} - \widehat{\widetilde{u}}_i\widehat{\widetilde{u}}_j\right)^{\mathrm{d}}, \quad (5)$$

$$q_j = \gamma\overline{\rho}\kappa_{\mathrm{sgs}}\partial_{x_j}\widetilde{e}_I - \gamma\overline{\rho}\left(\widehat{\widetilde{e}_I\widetilde{u}_j} - \widehat{\widetilde{e}}_I\widehat{\widetilde{u}}_j\right), \quad (6)$$

where $\widetilde{e}_I$ is the resolved internal energy and the *hat* operator represents filtering at cutoff length $1.5\Delta_{\mathrm{g}}$, where Δ_{g} is a measure of the actual grid resolution. Explicit filtering is performed using newly developed operators of arbitrary order (Lodato *et al.*, 2013) The SGS viscosity ν_{sgs} is computed with the WALE model (Nicoud & Ducros, 1999) and $\kappa_{\mathrm{sgs}} = \nu_{\mathrm{sgs}}/Pr_{\mathrm{sgs}}$ with $Pr_{\mathrm{sgs}} = 0.5$. In particular, the SGS scalar flux is approximated with an eddy-viscosity assumption as $q^c_j = \overline{\rho}\nu_{\mathrm{sgs}}/Sc_{\mathrm{sgs}}\partial_{x_j}\widetilde{c}$, with $Sc_{\mathrm{sgs}} = 0.5$.

The equations are integrated over an unstructured computational mesh of dimension $21D \times 12D \times 3.2D$ (L×H×W) with 35 760 unstructured hexahedral elements, and 4^3 solution points per element, thus giving a total number of DoF equal to 2.3×10^6.

The boundary conditions are periodic in the spanwise direction and no-slip isothermal conditions are used on the cylinder walls; the inflow/outflow conditions are imposed by fixing the inlet density and velocity and the outlet pressure, respectively, and the passive scalar emitted by a source term with a normal distribution centered at the release location to avoid discontinuities in the numerical solution.

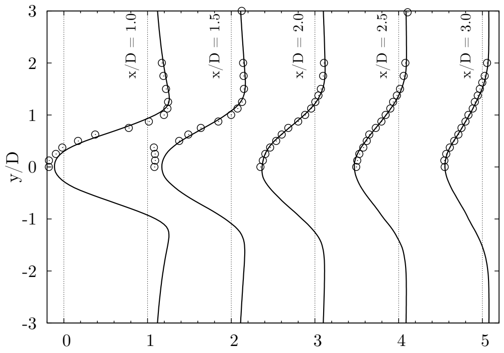

(a) $\langle u \rangle / U_\mathrm{b}$

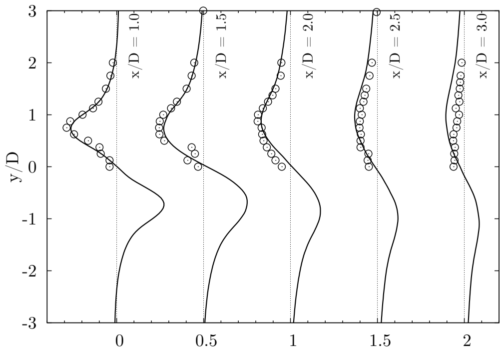

(b) $\langle v \rangle / U_\mathrm{b}$

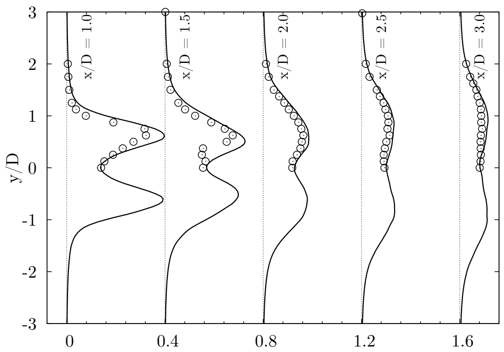

(c) $\langle u'u' \rangle / U_\mathrm{b}^2$

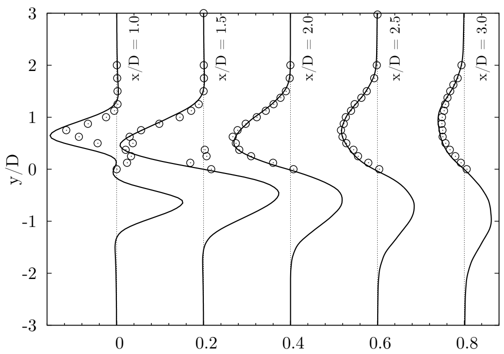

(d) $\langle u'v' \rangle / U_\mathrm{b}^2$

Figure 4. First- and second-order statistical moments of the resolved velocity field at different locations downstream of the square cylinder: —— , WSM model; ○ , experimental LDV measurements. Light dotted lines represent the zero location of the shifted curves.

LES VALIDATION

Before examining the mixing process of the scalar released by the point source, the flow field predicted by the present LES is validated against the LDV measurements by Lyn & Rodi (1994) and Lyn *et al.* (1995).

A first check of the accuracy of the LES methodology in capturing the dynamics of the coherent structures developing downstream of the cylinder was done by measuring the frequency of the shedding. The discrete Fourier transform of the time history of the lift coefficient is shown in Figure 3. The peak at the Strouhal number of 0.132 corresponds to the periodic shedding motion and matches perfectly the experimentally measured value of 0.132 ± 0.004, indicating that the wake dynamics is properly represented by the present LES. A detailed comparison of turbulence statistics downstream of the cylinder is presented next.

Time Averaged Statistics

Further validation of LES results is carried out by comparing the computed statistical moments of the velocity field with the available experimental counterparts. Hence, after the flow field was fully developed and established, statistics were collected in time for about 16 shedding periods, which for the present Reynolds number provided relatively well converged statistical samples; in view of the statistical two-dimensionality of the flow field, further ensemble averaging in the spanwise direction was also performed.

First- and second-order statistical moments at several locations downstream of the cylinder are plotted in Figure 4. An excellent agreement with measured data is seen for the mean streamwise velocity. The vertical velocity shows a slower decay when compared to the experiments at x/D=3. However, the uncertainty associated with measured data in this region must be high due to the reduced intensity of the vertical velocity component.

The profiles of the Reynolds stresses are also seen overall in very good agreement with the experimental data, even though the profile of $\langle u'v' \rangle$ does not present the secondary positive peak at x/D=1 near the symmetry plane shown by the measured profile. Nonetheless, the agreement of time-averaged statistics can be considered satisfactory.

Phase Averaged Statistics

In order to isolate the purely turbulent contribution from that of the organized periodic shedding motion, phase averaged statistics (Hussain & Reynolds, 1970) are computed for 8 equidistant phases within the shedding period. One time sample per period is collected for each phase over 120 shedding periods and averaging in the spanwise direction performed to increase the statistical samples for each phase to $40 \times 120 = 4800$.

Phases 1 and 7, which roughly correspond to phases 8 and 3 in the experimental measurements by Lyn & Rodi (1994) and Lyn *et al.* (1995), respectively, are presented in Figs. 5 and 6. Both the mean and turbulent profiles are found in good agreement with measured data, even though some of the local profiles do not match the conditionally-averaged LDV data. Since time-averaged statistics are seen in very good agreement with the experiments, the differences in the two dataset must be due to the limited number of samples available from LES as well as to the uncertainty associated with matching the location of the relevant phases in the experiments along the shedding cycle.

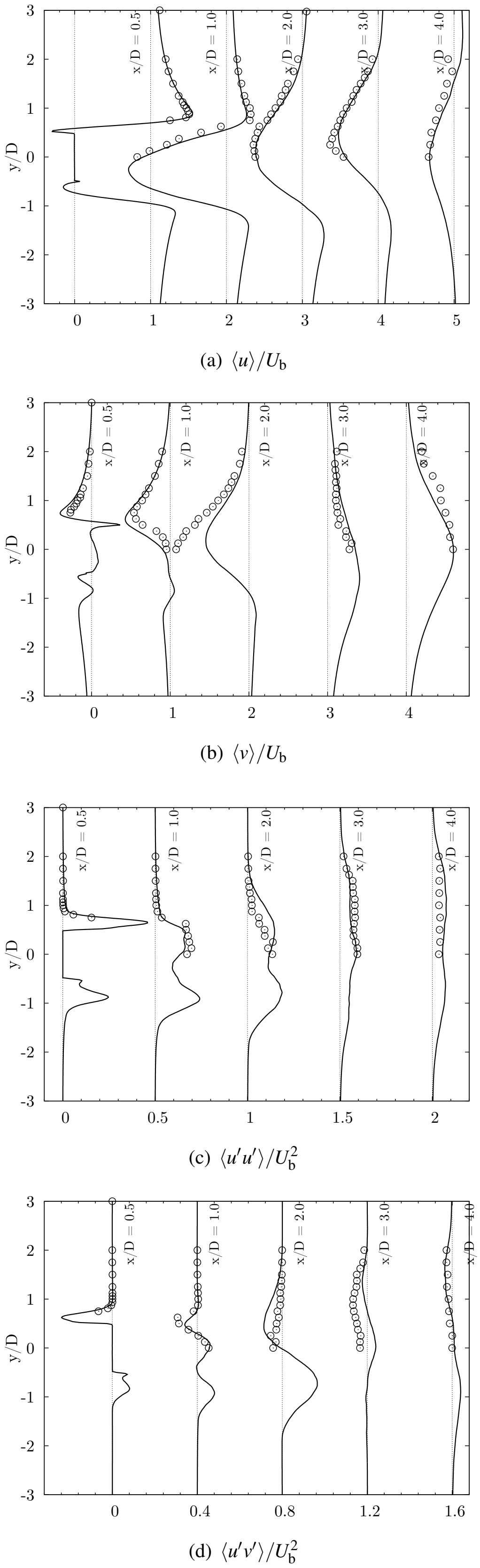

(a) $\langle u\rangle/U_\mathrm{b}$

(b) $\langle v\rangle/U_\mathrm{b}$

(c) $\langle u'u'\rangle/U_\mathrm{b}^2$

(d) $\langle u'v'\rangle/U_\mathrm{b}^2$

Figure 5. Phase 1 statistical moments of the resolved velocity field at different locations downstream of the square cylinder: —— , WSM model; ○ , experimental LDV measurements. Light dotted lines represent the zero location of the shifted curves.

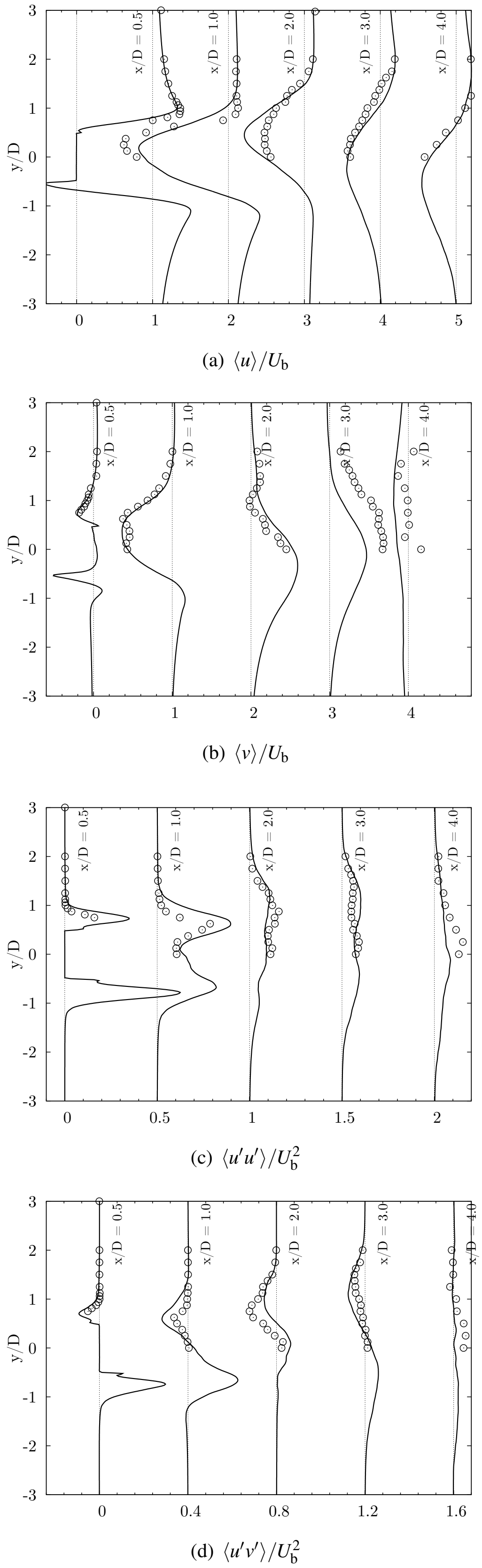

(a) $\langle u\rangle/U_\mathrm{b}$

(b) $\langle v\rangle/U_\mathrm{b}$

(c) $\langle u'u'\rangle/U_\mathrm{b}^2$

(d) $\langle u'v'\rangle/U_\mathrm{b}^2$

Figure 6. Phase 7 statistical moments of the resolved velocity field at different locations downstream of the square cylinder: —— , WSM model; ○ , experimental LDV measurements. Light dotted lines represent the zero location of the shifted curves.

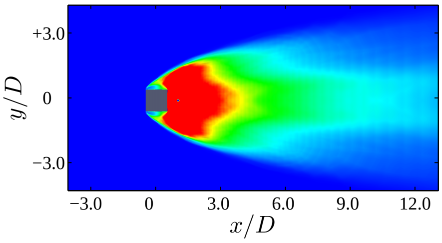

(a) $\langle c'^2 \rangle / C$

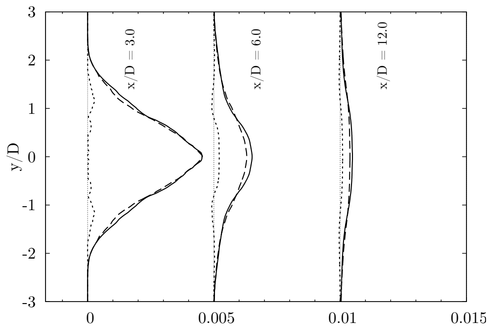

(b) $\langle c'^2 \rangle / C_{\max}$

Figure 7. Scalar variance: top, contour map, range $0 \div 1 \times 10^{-1}$; bottom, vertical profiles; – – – , random component, · · · · , periodic component.

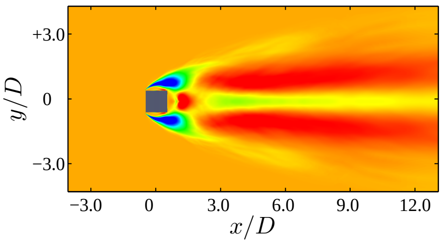

(a) $\langle u'c' \rangle / U_b C$

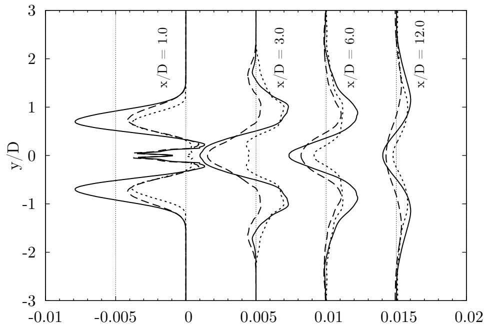

(b) $\langle u'c' \rangle / U_b C_{\max}$

Figure 8. Streamwise component of scalar flux: top, contour map, range $-5 \times 10^{-1} \div 1 \times 10^{-1}$; bottom, vertical profiles; – – – , random component, · · · · , periodic component. The profile at x/D=1 is scaled down by a factor of 5 in order to fit in the plot.

SCALAR FIELD ANALYSIS

Turbulence statistics for the scalar field are presented in Figs. 7-9, where C denote the local mean scalar concentration and $C_{\max}$ the maximum concentration at the source. The contour map of scalar variance, shown in Fig. 7(a), presents peak values of scalar fluctuations in the region immediately downstream of the cylinder, where the alternated formation of coherent vortical structures takes place. High-levels of scalar fluctuations also extend outside the cylinder width, reaching the two regions where the shear layers detaching from the leading edges of the bluff body roll up.

From the vertical profiles of the phase-averaged statistics in Fig. 7(b), it is seen that the scalar variance is dominated by random fluctuations in the wake of the cylinder. Near the source location, x/D=3, the fraction of scalar fluctuations associated with coherent motions is practically zero on the symmetry plane, whereas some contribution can be seen at $y/D \pm 1$, forming most probably the remainder of the two shear layers detaching initially from the cylinder. Farther downstream in the wake, coherent fluctuations play some role in producing the scalar variance on the symmetry plane, but the contribution is almost negligeable compared to the random component. This picture is consistent with the relatively high Reynolds number of the present flow setup and with the measurements reported by Godard *et al.* (2005) for a laminar wake, where scalar fluctuations were induced by periodic oscillations only, and those for a transitional wake at $Re_d \approx 5800$ reported by Matsumura & Antonia (1993), where the contribution from the coherent structures was found reduced to 23% of total scalar fluctuations.

Scalar flux components are presented in Figs. 8 and 9. The analysis of the contour map of the streamwise component shown in Fig. 8(a) against that of the gradient of mean concentration, not shown here for the sake of space, reveals that a counter-gradient transport occurs both on the symmetry plane immediately downstream of the source and in the two regions above and below the source, where the vortex-shedding builds up. From the vertical profile of the streamwise flux at $x/h = 1$, shown in 8(b), a significant contribution from coherent fluctuations is found in the region of counter-gradient transport, suggesting that such mechanism is driven by the correlation between the periodic fluctuations of the scalar and of the streamwise velocity, in agreement with previous studies reported in the literature (Paranthoën *et al.*, 2004). Nonetheless, on the symmetry plane the negative peak associated with the counter-gradient mechanism is dominated by random fluctuations, making the present scenario less clear than in the case of laminar and transitional wakes (Godard *et al.*, 2005; Matsumura & Antonia, 1993). The profiles also show that periodic fluctuations contribute mostly to the production of positive peaks in the streamwise flux downstream of the source.

The contour map of the vertical flux in Fig. 9(a) does not present any region of significant counter-gradient transport. Periodic and random components, shown in 9(b) contribute equally, overall, to the vertical flux. However, while random fluctuations build up the vertical flux taking place at the edge of the wake region, $y/D \pm 1.5$ at x/D=3, periodic fluctuations dominate the turbulent transport near the symmetry plane.

SUMMARY

Numerical experiments performed by LES on the turbulent flow and mixing of a passive scalar past a square cylinder have been presented. The scalar is released from a point source located in the mean separated region behind the cylinder, where vortex-shedding takes place, and then passively convected in the turbulent wake.

The validation study against LDV measurements per-

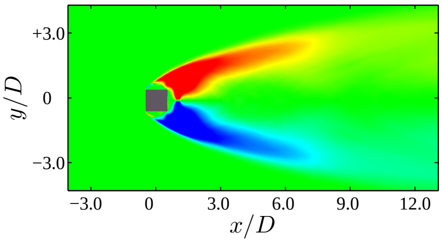

(a) $\langle v'c' \rangle / U_b C$

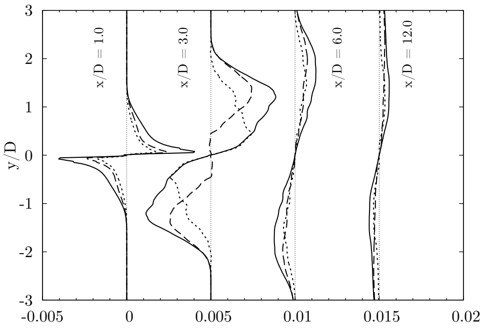

(b) $\langle v'c' \rangle / U_b C_{max}$

Figure 9. Vertical component of scalar flux: top, contour map, range $-2.5 \times 10^{-1} \div 2.5 \times 10^{-1}$; bottom, vertical profiles; $---$, random component, $\cdots\cdot$, periodic component. The profile at x/D=1 is scaled down by a factor of 50 in order to fit in the plot.

formed for the LES model employed in the analysis, where subgrid turbulent stresses are estimated via the WALE similarity mixed model coupled with newly developed constrained filtering operators of arbitrary order and scalar fluxes modeled via the Reynolds analogy, shows very good agreement with measured data for time-averaged and phase-averaged statistics of the velocity field.

The analysis of scalar field statistics, including scalar variance and scalar flux components, reveals that despite the relatively high Reynolds number of the present flow setup, coherent structures developing in the wake of the cylinder have a significant impact on the mixing process via the turbulent scalar flux components, representing, overall, half of the intensity of turbulent transport. Moreover, coherent structures are responsible for inducing a counter-diffusion mechanism in the streamwise component of the scalar flux. The present database will be used next in the analysis of scalar transport models in the framework of the RANS equations.

REFERENCES

Bosch, G & Rodi, W 1998 Simulation of vortex shedding past a square cylinder with different turbulence models. *Int. J. Numer. Meth. Fl.* **28** (4), 601–616.

Brown, S.T. 1987 Concentration prediction for meandering plumes based on probability theory. *Atmos. Environ.* **21** (6), 1321–1330.

Djenidi, L. & Antonia, R.A. 2009 Momentum and heat transport in a three-dimensional transitional wake of a heated square cylinder. *J. Fluid Mech.* **640**, 109–129.

Godard, G., Weiss, F., Paranthoën, P. & Gonzalez, M. 2005 Heat transfer from a line source located in the periodic laminar near wake of a circular cylinder. *Exp. Therm. Fluid Sci.* **29**, 956–947.

Hussain, A.K.M.F. & Reynolds, W.C. 1970 The mechanics of an organized wave in turbulent shear flow. *J. Fluid Mech.* **41** (2), 241–258.

Huynh, H.T. 2007 A flux reconstruction approach to high-order schemes including discontinuous Galerkin methods. *AIAA P.* **2007-4079**, 1–42.

Lakehal, D. & Thiele, F. 2000 Sensitivity of turbulent shedding flows to non-linear stress–strain relations and Reynolds stress models. *Comput. Fluids* **30** (1), 1–35.

Liang, C., Jameson, A. & Wang, Z.J. 2009 Spectral difference method for compressible flow on unstructured grids with mixed elements. *J. Comput. Phys.* **228**, 2847–2858.

Lodato, G., Castonguay, P. & Jameson, A. 2013 Discrete filter operators for large-eddy simulation using high-order spectral difference methods. *Int. J. Numer. Meth. Fl.* **72** (2), 231–258.

Lodato, G., Vervisch, L. & Domingo, P. 2009 A compressible wall-adapting similarity mixed model for Large-Eddy Simulation of the impinging round jet. *Phys. Fluids* **21** (3), 035102.

Lyn, D.A., Einav, S., Rodi, W. & Park, J.H. 1995 A laser-Doppler velocimetry study of ensemble-averaged characteristics of the turbulent near wake of a square cylinder. *J. Fluid Mech.* **304** (1), 285–319.

Lyn, D.A. & Rodi, W. 1994 The flapping shear layer formed by flow separation from the forward corner of a square cylinder. *J. Fluid Mech.* **267**, 353–376.

Matsumura, M & Antonia, R.A. 1993 Momentum and heat transport in the turbulent intermediate wake of a circular cylinder. *J. Fluid Mech.* **250** (1), 651–668.

Nicoud, F. & Ducros, F. 1999 Subgrid-scale stress modelling based on the square of the velocity gradient tensor. *Flow Turbul. Combust.* **62** (3), 183–200.

Paranthoën, P., Godard, G., Weiss, F. & Gonzalez, M. 2004 Counter gradient diffusion vs "counter diffusion" temperature profile? *Int. J. Heat Mass Tran.* **47**, 819–825.

Ramesh, V., Vengadesan, S. & Narasimhan, J.L. 2006 3D unsteady RANS simulation of turbulent flow over bluff body by non-linear model. *Int. J. Numer. Methods Heat Fluid Flow* **16** (6), 660–673.

Rossi, R. & Iaccarino, G. 2013 Numerical analysis and modeling of plume meandering in passive scalar dispersion downstream of a wall-mounted cube. *Int. J. Heat Fluid Fl.* **in press**.

Sun, Y., Wang, Z.J. & Liu, Y. 2007 High-order multidomain spectral difference method for the Navier-Stokes equations on unstructured hexahedral grids. *Commun. Comput. Phys.* **2** (2), 310–333.

Tsunoda, H, Sakai, Y, Nakamura, I & Liu, S 1993 The effect of a circular cylinder on the diffusion of matter by a plume. *J. Fluid Mech.* **246**, 419–419.

Vincent, P.E., Castonguay, P. & Jameson, A. 2010 A new class of high-order energy stable flux reconstruction schemes. *J. Sci. Comput.* **47** (1), 1–23.

Yiu, M.W., Zhou, Y & Zhu, Y 2004 Passive scalar transport in a turbulent cylinder wake in the presence of a downstream cylinder. *Flow Turbul. Combust.* **72** (2–4), 449–461.